ORIGINAL ARTICLE

lajss.org
Latin American Journal of Solids and Structures

www.lajss.org

Experimental study on the seismic behavior of RC columns improved with central large-diameter butted steel rods

Hanming Zhang[a,b], Jie Luo[c], Jianchun Xiao[a,b*], Jing Chen[a,b], Zhuoqun Liu[a,b], Yi Zhang[c], Zongli Luo[c], Hong Zhang[d]

[a] Research Center of Space Structures, Guizhou University, Guiyang 550025, China. Email: zhm_gzu@163.com, jcxiao@gzu.edu.cn, jchen23@gzu.edu.cn, Liu_zhuoqun@163.com

[b] Key Laboratory of Structural Engineering of Guizhou Province, Guiyang 550025, China.

[c] No.6 company of China Construction Fourth Engineering Bureau, Hefei 230011, China. Email: Lj_zjsj@163.com, zy_zjsj@163.com, lzl_zjsj@163.com

[d] Bureau of Housing and Urban-Rural Development of Wudang District, Guiyang 550018, China. Email: zh_wdzjj@163.com

* Corresponding author

https://doi.org/10.1590/1679-78257290

Abstract

A reinforced concrete (RC) column improved with central large-diameter butted steel rods (CLBSR column) has been proposed to increase the limit value of the axial compression ratio. This paper presents the seismic behavior analysis of CLBSR columns subjected to low-cycle reciprocating loading. The CLBSR columns were also compared with the RC column improved with central large-diameter steel rods (CLSR column) and the RC column improved with central reinforcement bars (CRB column) under the same experimental conditions. The typical failure modes, hysteretic curves, skeleton curves, stiffness degradation, and energy dissipation capacity were all investigated. The improved PARK damage model obtained the corresponding relationships between the damage indices and the damage state of each column. The test results indicated that the CLBSR columns and CLSR columns had similar seismic behavior, but were slightly inferior to the CRB columns. Overall, the butt joint of large-diameter steel rods had little effect on the seismic behavior.

Keywords

Large-diameter butted steel rods; seismic behavior; low-cycle reciprocating loading; hysteretic curve; PARK damage model.

Graphical Abstract

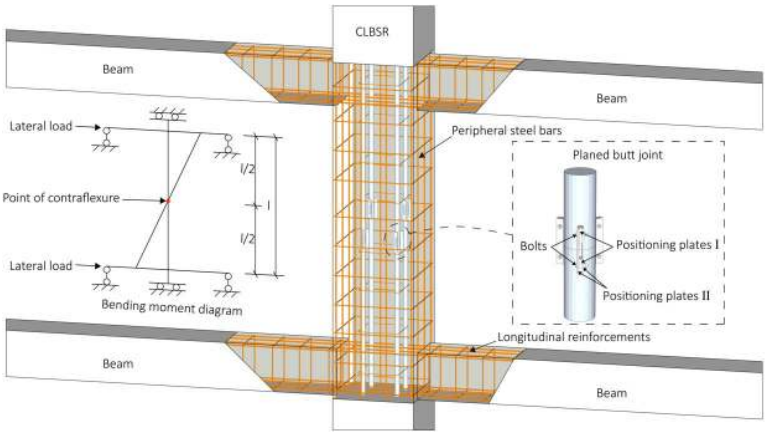

Received: September 12, 2022. In revised form: September 13, 2022. Accepted: September 19, 2022. Available online: September 20, 2022.
https://doi.org/10.1590/1679-78257290

Latin American Journal of Solids and Structures. ISSN 1679-7825. Copyright © 2022. This is an Open Access article distributed under the terms of the Creative Commons Attribution License, which permits unrestricted use, distribution, and reproduction in any medium, provided the original work is properly cited.

1 INTRODUCTION

Over the past decades, a series of RC columns improved with central reinforcing elements were proposed to increase the load bearing capacity and the ductility performance by offering additional constraints to concrete parts (Sakai et al. 2000). Many researchers have conducted lab tests and numerical analysis of the solid-web shaped steel reinforced concrete columns (SWSRC columns) due to its excellent seismic behavior and axial bearing capacity (Mostafa et al. 2019; Farajpourbonab. 2019). This is mainly because the solid-web shaped steels are not prone to buckling under the encasement of concrete, and the concrete in the core area can fully exhibit compressive behavior owing to the constraint effect of the solid-web steel (Denavit et al. 2018; Papavasileiou et al. 2020). Concrete-encased concrete-filled steel tubular column (CECFST column) is a typical type of composite column, in which steel tubes are added to the center of the columns (Wang et al. 2016). Steel tubes can fully restrain the concrete, thus giving the column prominent properties (Jothiman et al. 2019). Compared with conventional RC columns and CFST columns, CECFST columns demonstrate better corrosion and fire resistance due to the protection of the outer-layer concrete (Li et al. 2016; An et al. 2014; Lai et al. 2020).

Nevertheless, for the SWSRC and CECFST columns, the longitudinal reinforcements of the RC beam do not easy to pass through the beam-column joints, which limits their application in conventional buildings (Ma et al. 2018; Chinese code JGJ 138-2016; Wang et al. 2021). During the same period, the concrete-encased steel angle columns (CESA columns) and the RC columns improved with central reinforcement bars (CRB columns) were also proposed to provide an advisable solution to the problem of the complex construction process (Hwang et al. 2015; Kim et al. 2018; Lei et al. 2013; Xing et al. 2022). For the CESA column, the on-site construction had to connect the angles with steel plates to enhance the integrity of the core area. As for the CRB columns, more composite stirrups need to be added to the core, thus increasing the workload of steel bar tying. Therefore, Ye (Ye et al. 2012) reported an RC column improved with central large-diameter steel rods (CLSR column) to improve the axial bearing capacity of the conventional concrete columns, where the longitudinal reinforcements of the beam can easily penetrate the core region of the beam-column joint. As a practical example, the CLSR columns have been applied to the concrete outer frame of the Guangzhou Bank Building in China, in which the large-diameter steel rods were arranged in the compressive columns located in the 1~60 layers of the buildings (Zhao et al. 2011). Meanwhile, the connection of the large-diameter steel rods is not welded for facilitating construction. To investigate the seismic performance of the CLSR columns, Zhao (Zhao et al. 2012) conducted a low-cycle cyclic loading test of the CLSR columns and CECFST columns and the results reveal that the CLSR columns show similar seismic behavior to the CECFST columns.

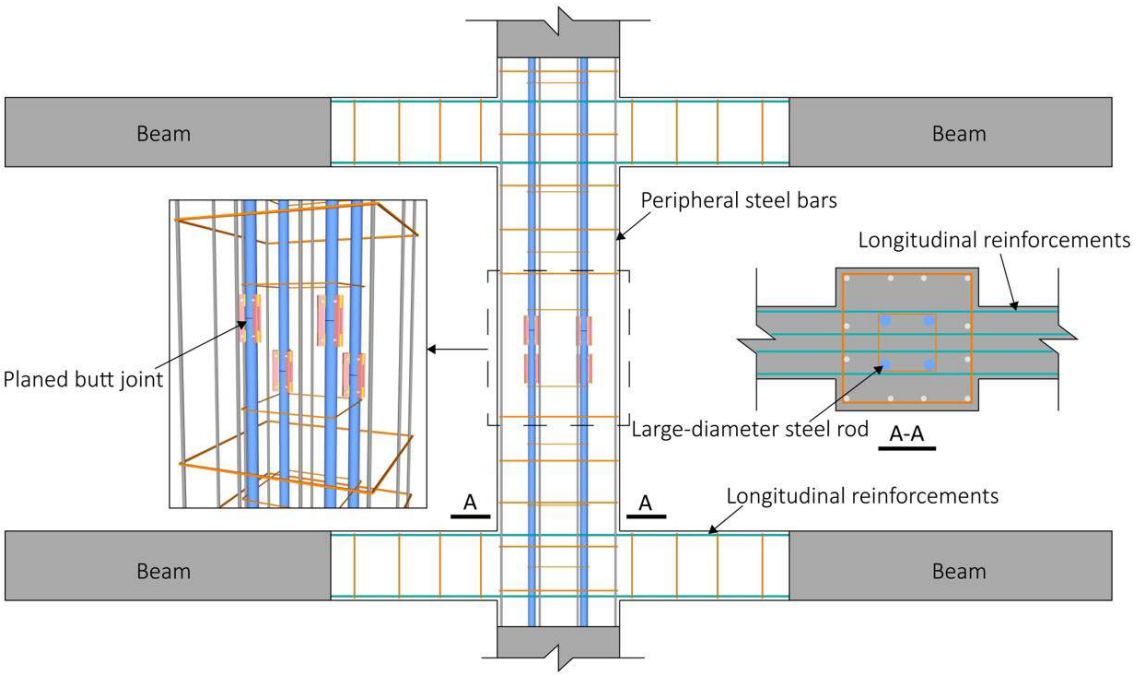

Figure 1 RC column improved with central large-diameter butted steel rods.

During the construction process of the CLSR columns, several shortcomings can be observed as follows: (1) the threads and sleeves on the ends of the large-diameter steel rods took more time to be prefabricated at the factory; (2)

the on-site connection of large-diameter steel rods required a high level of hoisting equipment. Therefore, the RC column improved with central large-diameter butted steel rods (CLBSR columns) was proposed to solve these problems, as shown in Fig. 1. The large-diameter steel rods are responsible for increasing the axial stiffness of the column. It is noteworthy that the steel rods were connected by planed butt joints, which are staggered near the contra flexure point to reduce the impact on the lateral stiffness of the column. The main function of the CLBSR columns was to bear vertical loads. To study the compressive performance of CLBSR columns, Chen (Chen 2012) firstly conducted the axial compression tests on four CLBSR columns. The results proved that the axial compressive capacity of CLBSR columns was about twice that of ordinary concrete columns. However, to the author's best knowledge, there is still a lack of research on the seismic performance of CLBSR columns. Therefore, this study aims to investigate the mechanical properties of CLBSR columns under low-cycle reciprocating loading and compare them with CLSR columns and CRB columns under the same experimental conditions. The failure processes, the hysteretic characteristics, the skeleton curves, the deformation capacity, the stiffness degradation, and the energy dissipation capacity are all incorporated in this paper. To predict the damage evolution of the tested columns, an improved PARK damage model was applied.

2 ENGINEERING BACKGROUND

As shown in Fig. 2, the Tower A of the Guiyang World Trade Center in Guizhou Province, China is an RC frame-core tube structure. The total height of Tower A was 380.95 m, including two subterranean floors and 77 aboveground floors. The building area was 226,000 m^2. The structural site belonged to category one. The seismic fortification intensity was six degrees. The seismic level of the frame was the first level. For the frame-core tube structure, the core tube usually bears more than 85% of the shear force, thus becoming the first line of defense against earthquakes (Chinese code JGJ 3-2010). The CLBSR columns have been applied in the concrete outer frame of the -2F to 42F, mainly playing the role of bearing vertical loads. In the CLBSR columns, the single steel rod was 100 mm in diameter. Its length was equal to the height of the standard layer. The flatness deviation of the end faces of the steel rods was less than 0.2 mm. The alignment error of the upper and lower steel rods was less than 1 mm. The verticality deviation was lower than 2 mm. The butt joints of steel rods were arranged at 1.5 m to 2 m above each floor, which avoids locations with large bending moments. To reduce the impact on the lateral stiffness of the column, the butt joint rate of steel rods on the same cross-section was less than 50%.

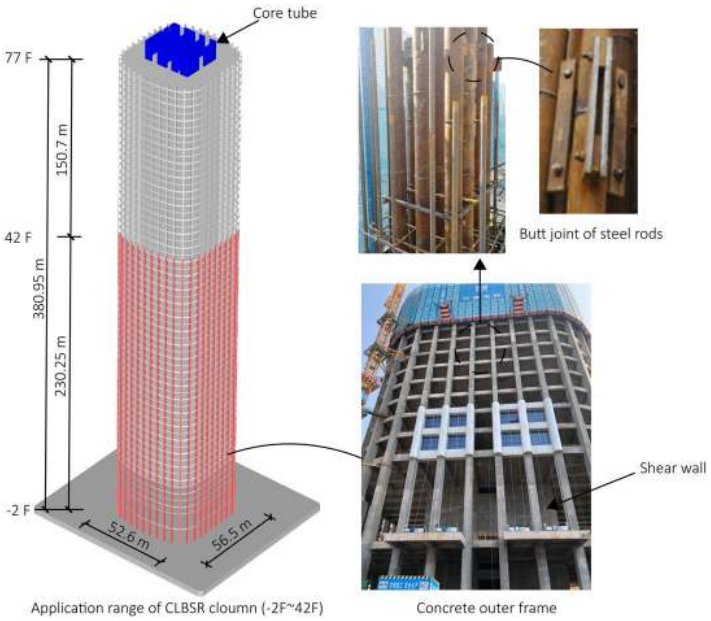

Figure 2 Application of CLBSR columns.

3 TEST PROGRAM

3.1 Test specimens

The scale of the specimens was determined to be 1/3 in the tests. As shown in Fig. 3, the height of all test specimens is 2100 mm. The size of the column cross-section was 300 mm × 300 mm, and the central reinforced area was 120 mm ×

120 mm. A reinforced concrete stub footing with a size of 900 mm × 500 mm × 300 mm was used to restrain the column. In addition, to reproduce the boundary conditions as accurately as possible, a reinforced concrete column head of size 500 mm × 400 mm × 300 mm was set. The details of all specimens are shown in Table 1, where H is the total height. b is the width of the column cross-section. h is the height of the column cross-section. n is the axial compression ratio, defined as $N/(f_c A_c + f_{ycre} A_{cre} + f_{ypsb} A_{psb})$ (Chen 2012), where N is the applied axial compressive load, f_c is the compressive strength of concrete, f_{ycre} is the yield strength of central reinforced elements, f_{ypsb} is the yield strength of peripheral steel bars, A_c is the area of column cross-section, A_{cre} is the area of central reinforcing elements, and A_{psb} is the area of peripheral steel bars.

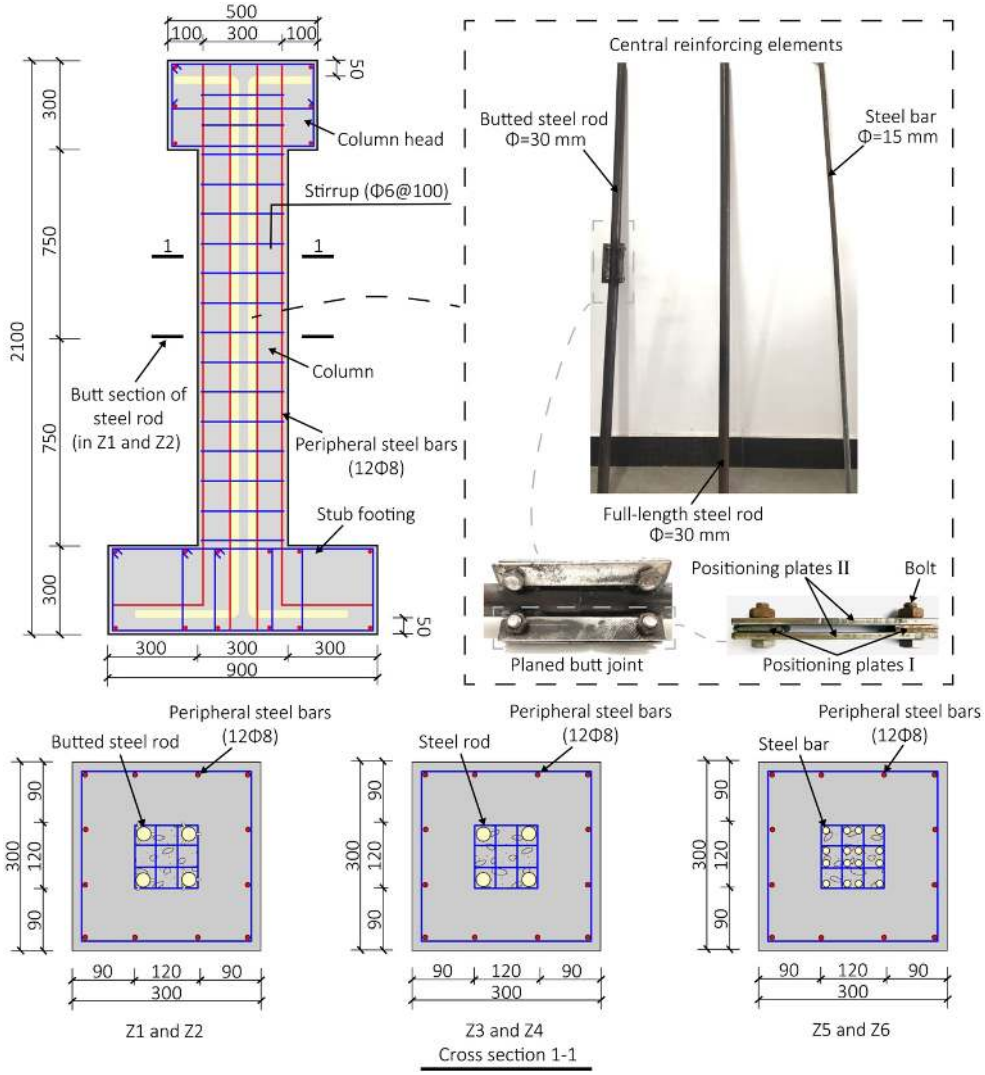

Figure 3 Application of CLBSR columns.

Table 1 Details of specimens.

Type	Specimen	Central reinforcing element	*H*(mm)	*b*(mm)	*h*(mm)	*n*
CLBSR	Z1	Butted steel rod (4Φ30)	2100.0	300.0	300.5	0.2
	Z2	Butted Steel rod (4Φ30)	2101.0	300.0	300.0	0.4
CLSR	Z3	Steel rod (4Φ30)	2100.0	300.0	300.0	0.2
	Z4	Steel rod (4Φ30)	2100.5	301.0	300.5	0.4
CRB	Z5	Steel bar (16Φ15)	2100.0	300.0	301.0	0.2
	Z6	Steel bar (16Φ15)	2101.0	300.0	300.0	0.4

The steel content of the central reinforced area of all columns was the same. The central reinforcing elements were embedded in the stub footing and column head but terminated at 50 mm from the ends of the specimen. For the butted steel rods, the end faces were planed with the precision of tolerance level IT, which represents a flatness deviation of 0.2 mm and a roughness of 12.5μm (Chinese code GB 50010-2010). The dimensional details of the planed butt joint are shown in Fig. 4.

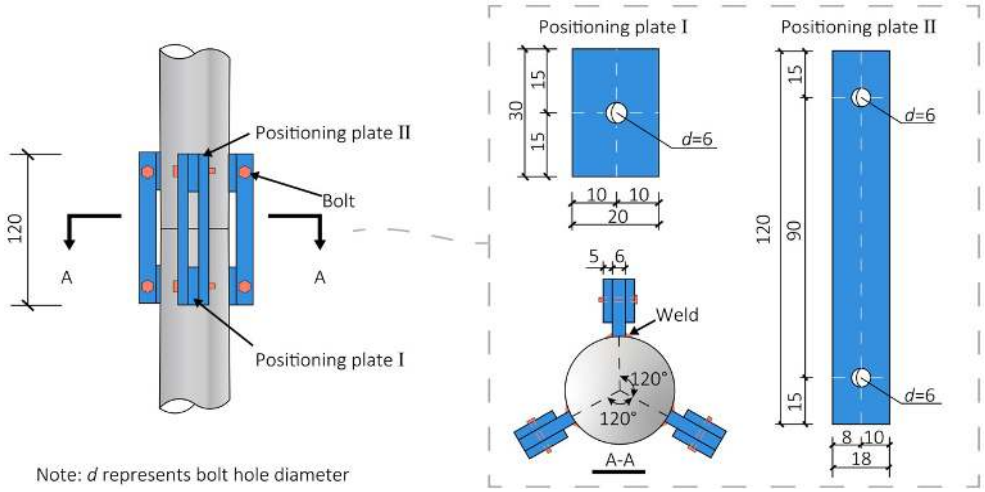

Figure 4 Dimensional details of planed butt joint.

3.2 Material properties

The design strength of concrete is C30, and its mix proportion was shown in Table 2. Among them, water was 10℃ tap water from the laboratory. The cement was ordinary Portland cement with a 28-day compressive strength of 42.5Mpa. As the fine aggregate, the sand was medium sand with a fineness modulus of 2.4, and its particle size ranged from 0.3 to 0.5 mm. As the coarse aggregate, the natural crushed stone was continuously graded and in a size range of 5~14 mm. The sulfonated naphthalene formaldehyde superplasticizer was provided by Shanxi Yellow River Admixture Factory in China.

Table 2 Mix proportion of concrete.

Water	42.5P.O. Cement	Sand	Gravel	Superplasticizer (%)
0.35	1	1.5	2.5	0.3

According to Chinese code GB 50010-2010 (China, 2010), the 150 mm × 150 mm × 150 mm standard cube blocks were prepared and cured under the same conditions as the specimens. The standard compressive strength f_c and elastic modulus E of the concrete were measured to be 36.6 MPa and 3.07 × 10^4 MPa, respectively. Following the standard ASTM A370 (US, 2017) the mechanical properties of the applied steel parts were measured as shown in Table 3.

Table 3 Mechanical properties of steel materials.

Type	Component	Diameter or thickness/mm	f_y/MPa	f_u/MPa	E_s/GPa
HPB300	Stirrup	6	320	433	214
	Peripheral steel bar	8	315	421	212
	Central steel bar	15	323	427	211
Q345B	Central steel rod	30	420	560	206
	Positioning plate I	6	390	555	211
	Positioning plate II	5	387	549	208
Class 4.8	Bolt	6	281	382	204

Note: f_y is the yield strength. f_u is the ultimate strength. E_s is the elastic modulus.

3.3 Test setup and instrumentation layout

The seismic behavior of the column was tested under the combined action of constant axial compressive load and lateral cyclic load. As shown in Fig. 5, the test setup consisted of a horizontal reaction system supporting the actuator (MTS-500KN) and a vertical reaction system supporting the hydraulic jack (HJ-250KN). The constant axial compression load and lateral cyclic load were provided by the hydraulic jack and the MTS actuator, respectively. To prevent sliding during the loading process, the specimen was fixed to the rigid ground using anchor rods. Simultaneously, the steel rollers were located between the pressure sensor and the specimen, which ensured free movement of the column head along the lateral load direction. The tests were carried out in the Key Laboratory of Structural Engineering of Guizhou Province.

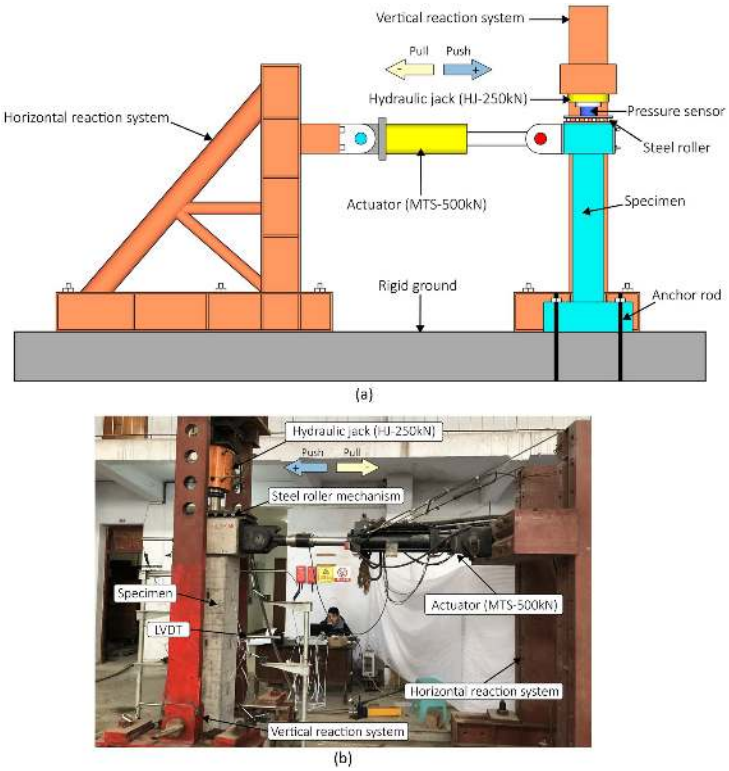

Figure 5 Test setup: (a) Model diagram; (b) Physical diagram.

As shown in Fig. 6, faces A, B and C were marked on the specimens, where faces A and C were perpendicular to the lateral load. Linear variable differential transformers (LVDTs) were placed along the height of the specimen. The lateral displacement of the loading point was measured by LVDT1. LVDT2- LVDT7 were used to monitor whether the column was twisted. LVDT8 was used to judge whether the stub footing moved. Strain gauges (SG1-SG16) were placed on the peripheral steel bars and the central reinforcing elements. During the test, the strain and displacement were collected by the TST3828EN data system. Meanwhile, the lateral load was collected by the MTS system.

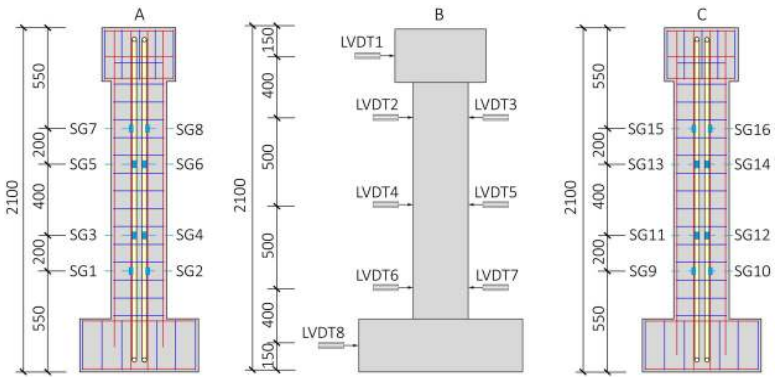

Figure 6 Layout of measuring points.

3.4 Loading procedure

According to the standard ASTM E2126-11 (US, 2018), all specimens were tested under displacement-controlled reversed cyclic load. The lateral loading protocol is shown in Fig. 7. Initially, the axial compressive load *N* was slowly applied to eliminate the inhomogeneity of the concrete. When reaching the required axial compression ratio, *N* was kept constant. Then, the lateral displacement δ was used to control the lateral load *F*. The first loading stage was carried out at displacement levels of 2 mm, 4 mm, 6 mm, 8 mm, and 10 mm, with only one cycle per displacement level. The initial displacement level of the second loading stage was 15 mm, and the next displacement level was increased by 5 mm until *F* decreased to 85% of the ultimate bearing capacity. In the second loading stage, the *i*-th displacement level was cycled three times.

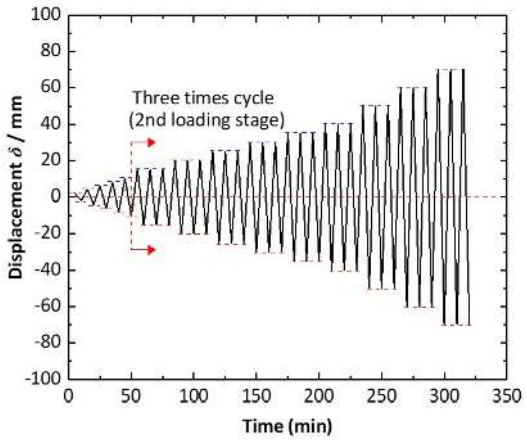

Figure 7 Lateral loading protocol.

4 TEST RESULTS AND DISCUSSION

4.1 Failure mode of columns

Fig 8 depicts the typical failure modes of the test columns. There are some similar characteristics for all columns, mainly including the following: (1) There was no significant change in the surface of the column during the application of the axial compression load. (2) in the first lateral loading stage, the first crack appeared within 200mm from the upper surface of the stub footing. For the columns with the same central reinforcing elements, the increasing height of the first crack occurs with the increased axial compression ratio. (3) as the lateral displacement δ increased, the peripheral steel bars reached yield first, accompanied by the fracture sound of the concrete. (4) when the columns failed, the cover concrete was severely spalled, and the peripheral steel bars were deformed by bending.

In particular, the CLBSR columns and the CLSR columns exhibited similar failure mechanisms. When δ < 7 mm, the columns were in an elastic state. Meanwhile, the first cracks appeared in the range of 180 ~ 200 mm from the upper surface of the stub footings. When δ reached 7 ~ 10 mm, the peripheral steel bars yielded. At the same time, the central reinforcing elements began to bear lateral loads. When δ reached 15 ~ 20 mm, the first cracks penetrated the column cross sections. When δ reached 20 ~30 mm, a few oblique cracks appeared at the lower corners of the columns. When δ reached 35 ~ 50 mm, the concrete at the lower corners began to crumble and spall, indicating the formation of plastic hinges at the lower ends of the columns. After δ reached 60 mm, the lateral load dropped to 85% of the ultimate load. In addition, the protection layer at the lower ends of the columns spalled off, resulting in exposure of the bent peripheral steel bars. These phenomena indicated the column failure.

Under the same axial compression ratio, the cracking, yield, and failure displacements were similar for the three types of columns. When the columns failed, the ends of the CLBSR and CLSR columns appeared hollow. Instead, the lower ends of the CRB columns were almost intact. The main reason was that the central reinforcing elements of the CRB columns had a larger contact area with the confined concrete, which effectively protected the central area of the columns.

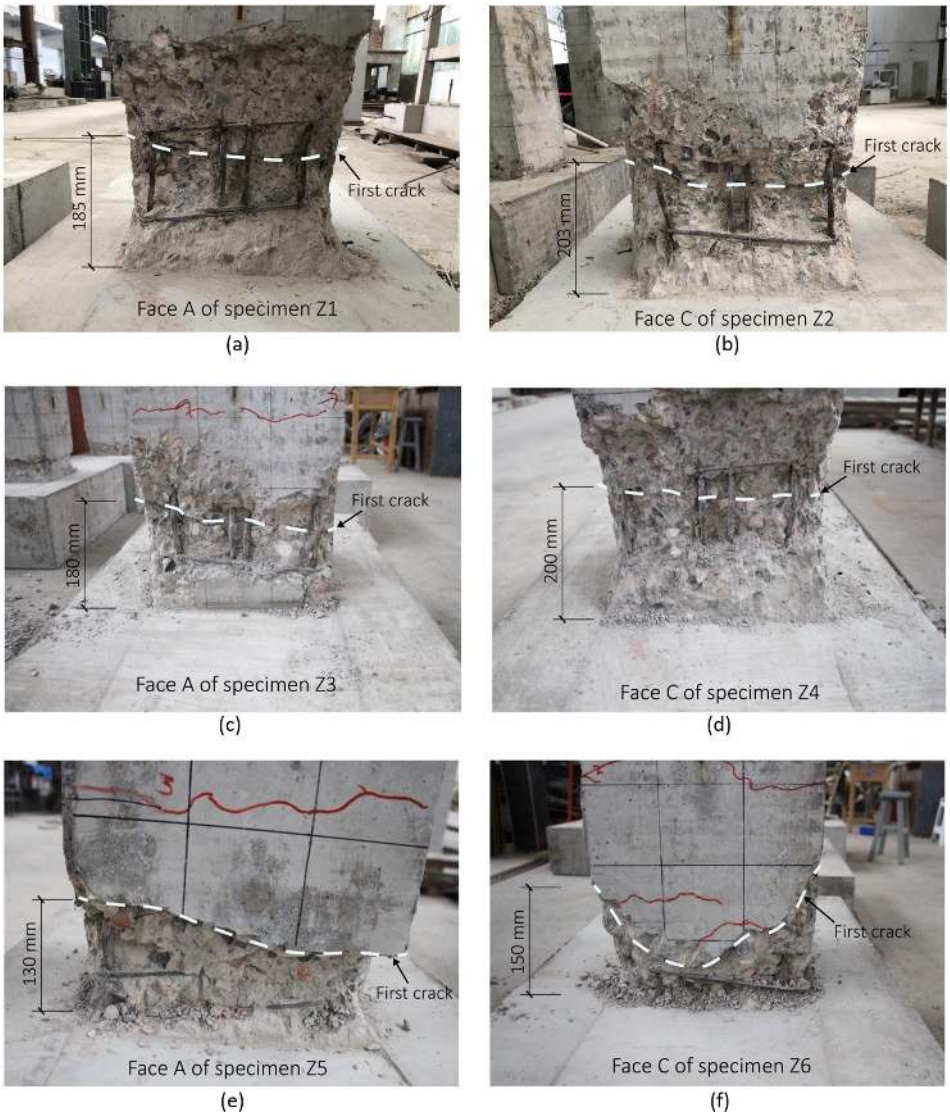

Figure 8 Failure modes of the test columns: (a) Z1; (b) Z2; (c) Z3; (d) Z4; (e) Z5; (f) Z6.

4.2 Hysteretic curves

The hysteretic relationship between lateral load F and lateral displacement δ at the loading point is shown in Fig. 9. The residual deformation of all specimens was small before the yielding of the peripheral steel bars. In the elastic stage, the area enclosed by each hysteresis curve was small, and the curve shape was fusiform. In the second loading stage, the hysteresis area of the first cycle was larger than that of the second cycle. After reaching the peak points, all curves shifted toward the displacement axis, indicating an obvious reduction in lateral stiffness. With increasing displacement, the hysteresis loop area continued to expand. The axial compression ratio had a significant effect on the hysteretic properties of the specimens. Under the same lateral displacement, the lateral loads of Z2, Z4, and Z6 were larger than those of Z1, Z3, and Z5, respectively, indicating that the bearing capacity of the same type of column increased with increasing axial compression ratio.

The curve shape, hysteresis loop area, and ultimate load of the CLBSR and CLSR columns were similar. There was no significant jitter in the curves of the CLBSR columns, indicating that the bonding between large-diameter butted steel rods and concrete was well maintained. The peak load and cumulative hysteretic loop area of the CRB columns were the largest among the three types of columns. This is because the central reinforcing elements of the CRB columns had a larger contact area with the concrete, which allows for better integrity of the central area in the CRB columns.

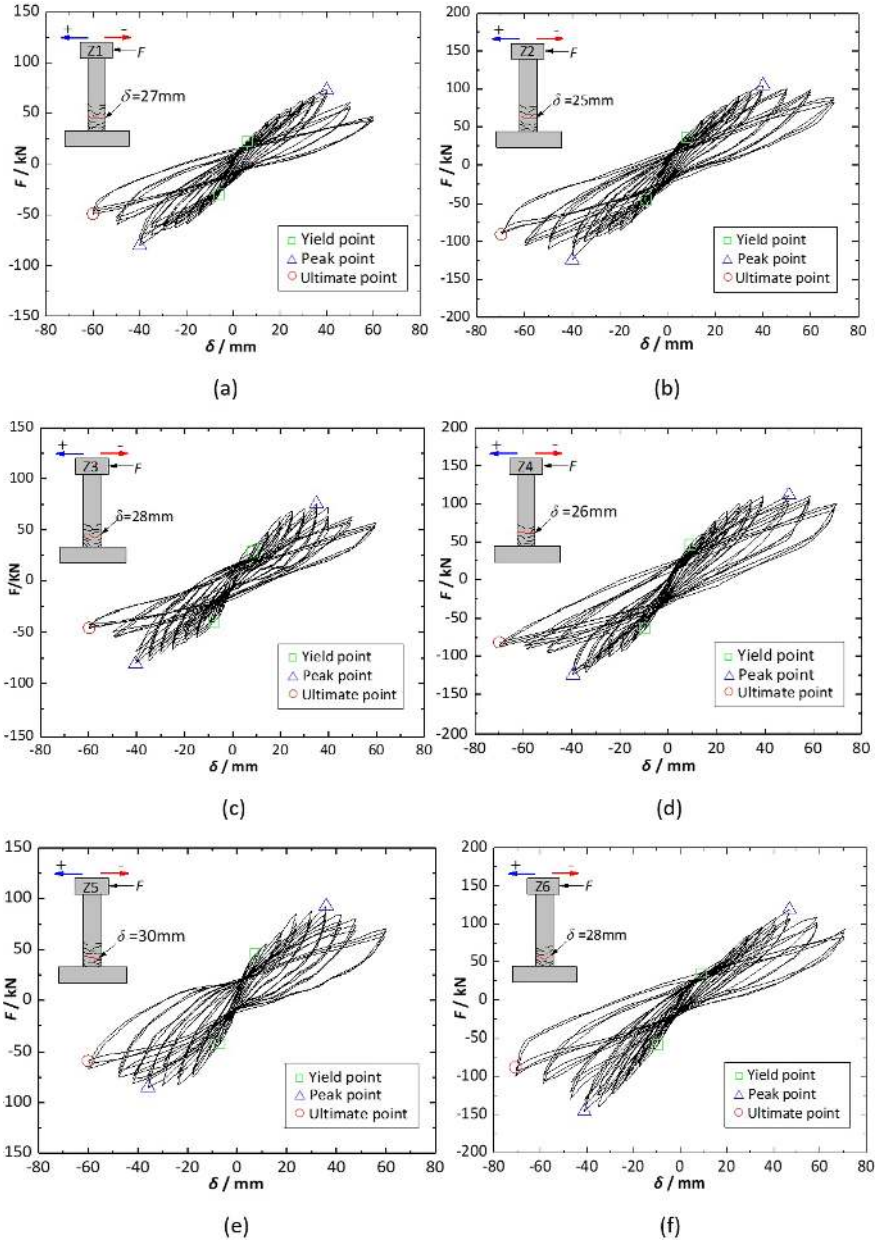

Figure 9 Hysteretic curves of columns.

4.3 Skeleton curves

The skeleton curve for each column is illustrated in Fig. 10. The cyclic loads of each specimen exhibited asymmetric characteristics because the mechanical properties of concrete were asymmetric on the one hand, and the bearing capacity was affected by cumulative damage on the other hand. Each curve tended to be linear under initial lateral loading, implying that the column was in the elastic range. The curves began to bend after reaching yield. As the axial compression ratio increased, the initial stiffness of the same type of column increased significantly. The reason may be that the greater axial compression load enhanced the bond between the aggregates in the elastic stage so that the compressive performance of the concrete could be more fully exerted. At the same displacement, the lateral load of the CRB column was greater than that of the CLBSR and CLSR columns. This shows that the central steel bars contributed more to the lateral bearing capacity of RC columns compared to large-diameter steel rods. In addition, the difference in peak load between CLBSR and CLSR columns is less than 5% under the same axial compression load. It can be seen that the bearing capacity of the RC column is not significantly reduced by the butt joints of large-diameter steel rods relative to the CLSR column.

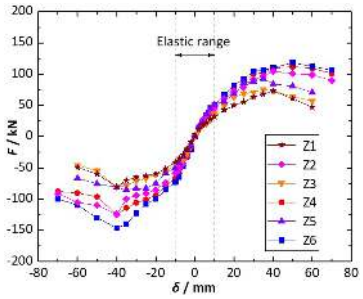

Figure 10 Skeleton curves of columns.

4.4 Bearing capacity and ductility

Four characteristic points, namely, the cracking point (F_{cr}, δ_{cr}), yield point (F_y, δ_y), peak point (F_p, δ_p), and ultimate point (F_u, δ_u), can be obtained from the skeleton curves. The loads and displacements of the characteristic points in different loading directions are summarized in Table 4. The characteristic loads F_{cr}, F_y, F_p, and F_u of the CLBSR and CLSR columns differed by 3%, 6%, 3%, and 8%, respectively. Under the same axial compression load, the bearing capacity of the CLBSR columns was close to that of the CLSR columns. This indicates that the butt joints of large-diameter steel rods had no significant effect on the bearing capacity of the column. Compared to the characteristic loads F_{cr}, F_y, F_p, and F_u of CRB columns, those of the CLBSR columns were relatively decreased by 17%, 22%, 14%, and 21%, respectively. For the columns with the same central reinforcing elements, the bearing capacity increased with increasing axial compression load. The ductility coefficient μ and drift ratio ϑ can determine the ductility and deformation capacity of a structure. They are defined as follows:

$$\mu = \delta_u / \delta_y \tag{1}$$

$$\theta = \delta_u / H_n \tag{2}$$

where H_n is the net height of the column (1500 mm). The calculation results of the ductility coefficient and limit drift ratio of each column are shown in Table 4.

Table 4 Experimental results of characteristic points.

Specimen	Loading direction	Crack		Yield		Peak		Ultimate		μ	ϑ
		F_{cr} (kN)	δ_{cr} (mm)	F_y (kN)	δ_y (mm)	F_p (kN)	δ_p (mm)	F_u (kN)	δ_u (mm)		
Z1	+	18.7	4.3	22.3	7.1	72.7	40.4	46.8	60.1	8.38	1/25
	-	25.6	4.8	31.3	7.3	80.1	39.9	48.9	59.9	8.17	1/25
Z2	+	33.1	6.2	39.8	8.9	104.5	40.5	89.7	69.8	7.78	1/21
	-	46.9	7.1	55.9	8.9	124.1	40.3	90.6	69.6	7.76	1/21
Z3	+	18.8	6.1	25.1	7.2	75.4	35.1	56.3	60.5	8.43	1/25
	-	24.1	6.8	34.3	7.3	80.7	39.9	45.3	60.2	8.21	1/25
Z4	+	35.0	7.4	40.3	8.9	111.1	49.8	99.8	69.9	7.83	1/21
	-	48.9	7.8	56.9	8.6	124.2	40.8	87.6	69.6	7.76	1/21
Z5	+	25.2	4.9	32.8	7.1	92.5	35.2	70.3	59.9	8.43	1/25
	-	34.8	5.2	41.3	7.2	85.1	35.1	66.4	59.8	8.31	1/25
Z6	+	36.4	6.7	47.9	8.8	118.4	49.7	106.2	70.6	8.02	1/21
	-	50.6	7.4	66.4	8.9	146.6	40.8	99.5	70.2	7.88	1/21

Note: "+" represents the push loading direction. "-" represents the pull loading direction. δ_{cr} is the crack displacement. δ_y is the yield displacement. δ_p is the displacement corresponding to the peak load. δ_u is the ultimate displacement.

The ductility coefficients of CLBSR columns were slightly inferior to those of the CLSR columns with a difference of 2%. As a result, the butt joints of large-diameter steel rods had little effect on the ductility and deformation capacity. Compared with CRB columns, the ductility of the CLBSR and CLSR columns decreased by 3% and 2% respectively. This

may be because the yielding of the central steel bars enhanced the overall deformation capacity of the CRB column. Under the same axial compression ratio, ϑ of the three types of columns was greater than the limit of 0.02 specified by the Chinese code GB 50011-2010 (China, 2010). Therefore, all columns had sufficient ductility. For columns with the same central reinforcing elements, as the axial compression load increased, the ductility decreased, while the limit drift ratio increased.

4.5 Strength degradation

The strength degradation coefficient implies that the strength decreases when the same displacement level is reached. At the *i*-th level displacement, the peak loads of the three cycles are marked as F_{i1}, F_{i2}, and F_{i3}. The first-order strength degradation coefficient is defined as $\lambda_{i1} = F_{i2} / F_{i1}$, and the second-order one is defined as $\lambda_{i2} = F_{i3} / F_{i2}$. The relationship between the strength degradation coefficient and the lateral displacement at the loading point is illustrated in Fig. 11.

In general, the strength degradation of reinforced concrete columns is caused by concrete cracking and yielding of steel bars. As the displacement increased, the strength of each column degraded faster. The degradation coefficients did not change significantly with increasing axial compression load. Therefore, the axial compression load had little effect on the cyclic behavior of each column. The strength degradation coefficients of all columns ranged from 0.9 to 1.0, which indicates that all columns had stable bearing capacity.

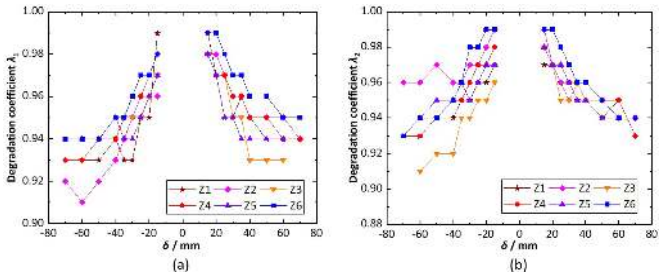

Figure 11 Strength degradation of each column: (a) first-order strength degradation coefficient; (b) second-order strength degradation coefficient.

4.6 Energy dissipation capacity

The energy dissipation capacity is measured by the area enclosed by the hysteretic curve. Fig 12a shows the cumulative energy dissipation process of each column. The relative energy dissipation E_r of each column was obtained by normalizing the energy dissipation of column Z1, as shown in Fig. 12b.

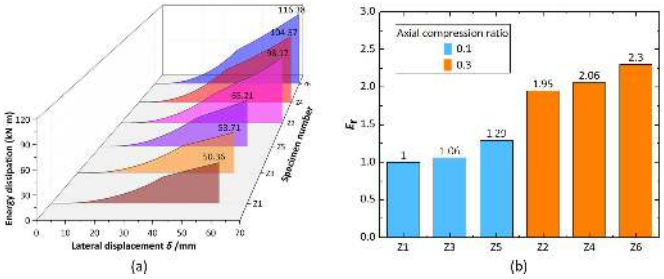

Figure 12 Energy dissipation of each column: (a) Energy dissipation process; (b) Relative energy dissipation E_r.

The equivalent viscous damping coefficient h_e is another indicator for evaluating the seismic energy dissipation, which is defined as:

$$h_e = \frac{1}{2\pi} \times \frac{S_{ABCD}}{\left(S_{OBE} + S_{ODH}\right)} \tag{3}$$

where S_{ABCD} represents the energy consumed during one cycle. S_{OBE} and S_{ODH} represent the energy consumed by the ideal elastic structure at the same displacement, as shown in Fig. 13. The calculation results of coefficient h_e at characteristic points are listed in Table 5.

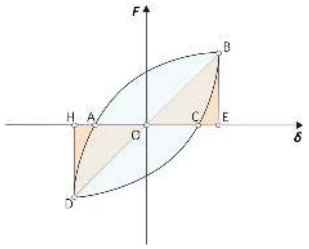

Figure 13 Calculation method for equivalent viscous damping coefficient.

Table 5 Experimental results of characteristic points.

Characteristic points	Specimens					
	Z1	Z2	Z3	Z4	Z5	Z6
Yield	0.007	0.009	0.008	0.008	0.013	0.011
Peak	0.074	0.093	0.088	0.105	0.094	0.135
Ultimate	0.105	0.128	0.109	0.139	0.127	0.151

The results of the energy dissipation and equivalent viscous damping coefficient were analyzed and the following key points are concluded: (1) As the displacement increased, the cumulative energy dissipation of each column increased continuously. In the elastic stage, the energy dissipation of each column was small. When entering the plastic stage, the cumulative energy dissipation increased rapidly. When the displacement δ_p was reached, the growth rate of cumulative energy dissipation became slower. (2) at the initial stage of loading (δ < 10 mm), there was almost no energy dissipation and the equivalent viscous damping coefficients were small. The coefficients h_e increased continuously with the loading displacement and reached the maximum values at the ultimate points. This indicated that the seismic performance of each column improved with increasing plastic deformation. (3) under the same axial compression load, the cumulative energy dissipation of the CLBSR and CLSR columns was reduced by 17% and 13%, respectively, compared to the CRB columns. Meanwhile, the equivalent viscous damping coefficients of the CRB columns were the largest among the three types of columns. These results demonstrated that the central reinforcing elements of the CRB column contributed more to the energy dissipation. The main reason was that the central reinforcing elements of the CRB columns had a larger contact area with the confined concrete, which provided better integrity in the central area of the column. (4) under the same axial compression load, the energy dissipation of the CLBSR columns was 5% less than that of the CLSR columns. The coefficients h_e of the CLBSR and CLSR columns were close at the same characteristic point. This result indicated that the butt joints of the steel rods had little effect on the energy dissipation capacity of the columns.

4.7 Stiffness degradation

Stiffness degradation reflects the crack development of the column and the plastic deformation of the material (Wang et al. 2022). According to the Chinese code GB 50011-2010, the lateral stiffness K_i of the column is calculated as:

$$K_i = \frac{\left|+F_i\right| + \left|-F_i\right|}{\left|+\delta_i\right| + \left|-\delta_i\right|} \tag{4}$$

where $+F_i$ is the peak load at the i-th level positive displacement $+\delta_i$. $-F_i$ is the peak load at the i-th level negative displacement $-\delta_i$. The stiffness degradation curve of each column is shown in Fig. 14, and the following conclusions are drawn: (1) When the lateral displacement was less than 10 mm, the stiffness degradation curves of all columns were steep. This was caused by cracking of the concrete and yielding of the peripheral steel bars. As the loading displacement increased, the slope of each stiffness degradation curve decreased, and the stiffness degradation speed became slower. (2) the stiffness of the specimens under higher axial compression ratios was greater. This indicated that the axial compression load restrained the specimen and improved the overall stiffness. However, a higher axial compression load also aggravated the damage accumulation of concrete, resulting in unsteady stiffness. (3) under the same axial compression load, the stiffness of both CLBSR and CLSR columns was smaller than that of CRB columns, which suggested that the type of central reinforcing

elements had a significant effect on the stiffnesses of the column. When reaching the peak stage, the stiffness of Z1 and Z3 tended to be the same. A similar phenomenon occurred between Z2 and Z4. It can be concluded that the butt joints of the central steel rods did not cause a sudden change in the stiffness of the column cross-section.

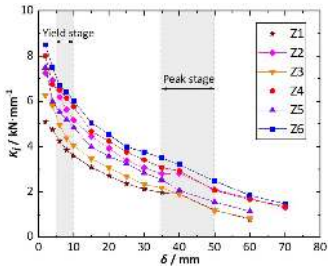

Figure 14 Stiffness degradation of each column.

4.8 Failure mechanism analysis

A strain monitoring system collected the strain of the measuring points in Fig. 6. The strain on the peripheral steel bars and the central reinforcing elements is shown in Fig. 15. Positive values represent tensile strain and negative values represent compressive strain. For all columns, the strain trends of the peripheral steel bars and the central reinforcing elements were similar. The central steel rods in the CLBSR and CLSR columns were mainly in compression. Although the central steel rods exhibited tensile strain, they did not yield in tension. When the loading displacement reached approximately 10mm, the strain of the central steel rods showed a sudden increase, indicating that the central steel rods and the peripheral steel bars bore the lateral load together. The strain of the central steel bars in the CRB columns monotonically increased, and finally reached compressive yield. This also contributed to improving the deformation capacity of the CRB column. As the displacement increased, the central reinforcing elements were extruded with concrete, and then worked together with the steel cage. Although the peripheral steel bars yielded, the central area of the column still resisted the lateral load. When failure occurred, the concrete at the lower ends of the CLBSR and CLSR columns spalled widely with hollowing phenomena. Instead, the lower ends of the CRB columns can remain intact.

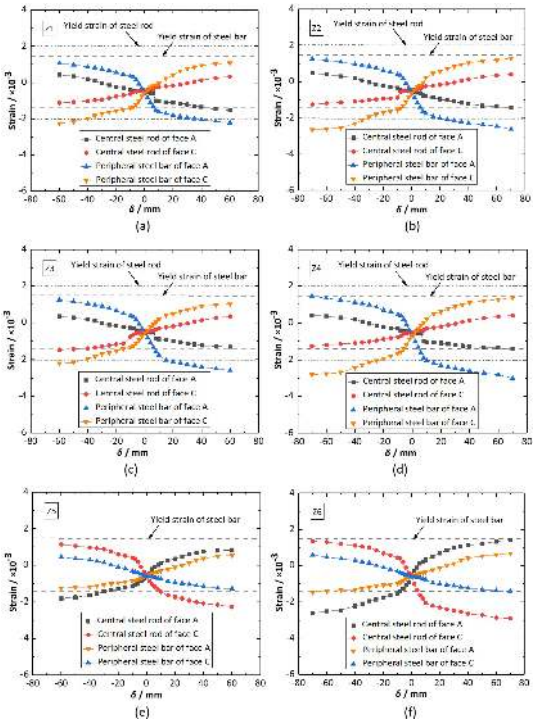

Figure 15 Strain of steel members: (a) Z1; (b) Z2; (c) Z3; (d) Z4; (e) Z5; (f) Z6.

5 ANALYSIS OF DAMAGE EVOLUTION

The damage index is a useful quantitative indicator for seismic behavior (Kamaris et al. 2016). Based on the linear combination of displacement and energy, PARK proposed a two-parameter seismic damage model (Park et al. 1985). The PARK damage index D is defined as:

$$D = \frac{\delta_{\mathrm{m}}}{\delta_{\mathrm{um}}} \times \frac{\beta \int \mathrm{d}E}{F_{\mathrm{y}} \delta_{\mathrm{um}}} \tag{5}$$

where δ_{m} is the maximum displacement under earthquake loading. δ_{um} is the ultimate displacement under monotonic loading. F_{y} is the yield load. dE is the incremental absorbed hysteretic energy. β is a nonnegative parameter.

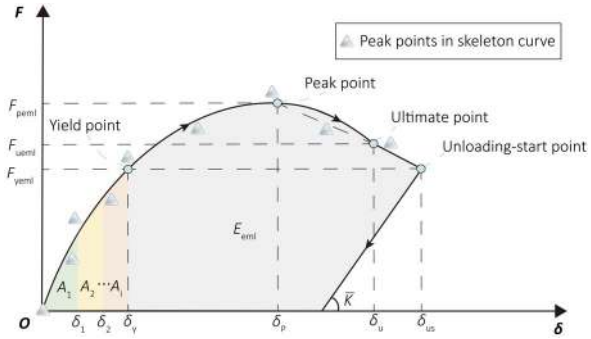

Figure 16 Energy dissipation of equivalent monotonic loading.

Generally, the abovementioned PARK model is built based on the results of the monotonic loading test (MLT). To avoid relying on MLT, Qi (Qi et al. 2016) proposed an improved PARK damage model, which can obtain an equivalent monotonic loading curve (EMLC) by fitting the peak points at all levels of displacement in the skeleton curve, as shown in Fig. 16. Formula (6) is introduced to determine this calculation method of the damage index.

$$D = \alpha \frac{\delta_{\mathrm{i}} - \delta_{\mathrm{cr}}}{\delta_{\mathrm{u}} - \delta_{\mathrm{cr}}} + \gamma \frac{\int \mathrm{d}E_{\mathrm{i}}}{E_{\mathrm{eml}}} \tag{6}$$

where α and γ are the coefficients of the displacement term and the energy term, respectively, and are determined by the damage boundary conditions ($\delta = 0$, $D = 0$; $\delta = \delta_{\mathrm{se}}$, $D = 1$). δ_{se} indicates the displacement when massive concrete spalls and steel bars are exposed. δ_{i} is the i-th level displacement. δ_{u} is the ultimate displacement under cyclic loading. δ_{cr} is the cracking displacement. dE_{i} is the cumulative energy dissipation at i-th level displacement. E_{eml} is the energy dissipation under equivalent monotonic loading. The load of the unloading-start point takes the yield load F_{yeml}, and the corresponding displacement is δ_{us}. The unloading stiffness $\overline{K}$ is the average of the stiffness before yield displacement δ_{y}. The parameters are expressed as follows:

$$\delta_{\mathrm{us}} = \delta_{\mathrm{u}} + \frac{F_{\mathrm{ueml}} - F_{\mathrm{yeml}}}{F_{\mathrm{peml}} - F_{\mathrm{ueml}}} \left(\delta_{\mathrm{u}} - \delta_{\mathrm{p}} \right) \tag{7}$$

$$\overline{K} = \sum_{\mathrm{i}=1}^{n} K_{\mathrm{i}} A_{\mathrm{i}} \Big/ \sum_{\mathrm{i}=1}^{n} A_{\mathrm{i}} \tag{8}$$

where K_{i} is the lateral stiffness at the i-th level displacement before reaching yield. A_{i} is the area enclosed by the equivalent monotonic loading curve at the i-th level displacement. The PARK damage model was listed in Formula (6) to solve the damage indices of each column at different displacement levels. The variation curves of the damage index D with the displacement δ are shown in Fig. 17. Then, the damage indices were compared with the test phenomenon to obtain the corresponding relationship between the damage index and the damage state, as shown in Table 6.

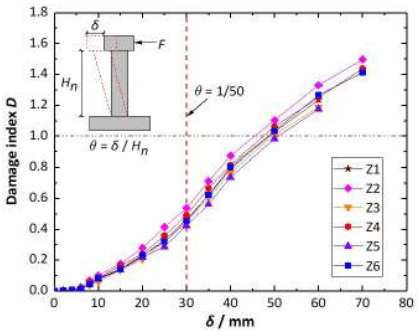

Figure 17 Energy dissipation of equivalent monotonic loading.

When the displacement δ was less than 10 mm, the damage indices of all columns were less than 0.1, indicating no serious damage occurred in the columns during the elastic stage. The damage indices rose continuously with increasing displacement. As the displacement increases, the accumulative damage gets worse. For the columns with the same central reinforcing elements, the damage index D was greater under a higher axial compression load. The main reason might be that the higher axial compression load accelerated the crushing of concrete and the compressive yielding of steel bars. Under the same axial compression load, the damage indices of the CLBSR and CLSR columns were similar, which implied that the butt joints of the central steel rods did not significantly affect the column damage. When the drift ratio ϑ reached the limit value of 1/50, the damage indices of the CLBSR, CLSR, and CRB columns ranged from 0.46 ~ 0.53, 0.44 ~ 0.49, and 0.42 ~ 0.45, respectively. Meanwhile, a moderate repair effort was required to extend the service life of these columns.

Table 6 Damage observed in the test and predicted damage state.

Column	Test cycle	Observation	Damage state	*D*	Repair level
Z1	6th	Concrete cracking and minor spalling	Minor	0.14	I
	16th	Steel bars exposing	Moderate	0.46	II
	26th	Column end hollowing	Collapse	1.0	III
Z2	7th	Concrete cracking and minor spalling	Minor	0.17	I
	15th	Steel bars exposing	Moderate	0.53	II
	24th	Column end hollowing	Collapse	1.0	III
Z3	8th	Concrete cracking and minor spalling	Minor	0.13	I
	17th	Steel bars exposing	Moderate	0.44	II
	26th	Column end hollowing	Collapse	1.0	III
Z4	7th	Concrete cracking and minor spalling	Minor	0.16	I
	15th	Steel bars exposing	Moderate	0.49	II
	24th	Column end hollowing	Collapse	1.0	III
Z5	8th	Concrete cracking and minor spalling	Minor	0.13	I
	17th	Steel bars exposing	Moderate	0.48	II
	26th	Concrete severe spalling	Collapse	1.0	III
Z6	10th	Concrete cracking and minor spalling	Minor	0.15	I
	19th	Steel bars exposing	Moderate	0.45	II
	29th	Concrete severe spalling	Collapse	1.0	III

Note: I indicates that the repair cost is less than 20% of the structural cost; II shows that the repair cost is between 20% and 60% of the structural cost; III denotes that the repair cost surpasses 60% of the structural cost.

6 CONCLUSIONS

Two CLBSR columns were tested under the combined action of constant axial compressive load and lateral cyclic load. The comparison between the CLBSR columns, the CLSR columns, and the CRB columns are all incorporated by lab

tests. An improved PARK damage model was used to analyze the damage evolution law of all columns. According to the research results, the following main conclusions are drawn:

(1) All columns exhibited bending failure under low-cycle reciprocating loading. For the columns with the same central reinforcing elements, the lateral stiffness, ultimate lateral bearing capacity, energy dissipation, and cumulative damage improved with increasing axial compression load, while the ductility dropped. When failure occurred, massive concrete at the lower ends of the CLBSR and CLSR columns spalled, accompanied by hollowing-out phenomena. The lower ends of the CRB columns remained intact in contrast. The central reinforcing elements of the CRB columns had a larger contact area with the confined concrete, which effectively protected the central area.

(2) Compared with the CRB columns, the bearing capacity of the CLBSR and CLSR columns decreased by 18% and 15%, respectively, the ductility coefficient decreased by 8% and 12%, and the energy dissipation capacity decreased by 17% and 13%, respectively. In contrast to CLSR columns, the lateral bearing capacity, ductility coefficient and cumulative energy dissipation of the CLBSR columns decreased by 5%, 2%, and 5%, respectively. Overall, the butt joint of large-diameter steel rods had little effect on the seismic behavior.

(3) When the drift ratio ϑ reached the limit value of 1/50, the damage indices of the CLBSR, CLSR, and CRB columns ranged from 0.46~0.53, 0.44~0.49, and 0.42~0.45, respectively. No serious damage occurred in all columns. A moderate repair effort was required to extend the service life of the columns.

Author's Contributions: *Conceptualization*, Han-Ming Zhang and Jian-Chun Xiao; *Methodology*, Han-Ming Zhang and Jie Luo; *Experiment*, Han-Ming Zhang, Jing Chen and Zhuo-Qun Liu; *Validation*, Han-Ming Zhang, Jian-Chun Xiao and Zhuo-Qun Liu; *Investigation*, Yi Zhang, Zong-li Luo and Hong Zhang; *Resources*, Jian-Chun Xiao and Jie Luo; *Data curation*, Han-Ming Zhang; *Writing—original draft preparation*, Han-Ming Zhang; *Visualization*, Han-Ming Zhang and Jing Chen; *Funding acquisition*, Jian-Chun Xiao.

Editor: Marcílio Alves

Conflicts of Interest: All authors declare no conflict of interest.

Funding: This research was funded by the National Natural Science Foundation of China contract No.50978064; Research Project Foundation of No.6 company of China Construction Fourth Engineering Bureau. Limited. ZJSJLGS-20181118; Guizhou Natural Science Foundation Program QRF-201701; Foundation of Guizhou University GZUF202034.

References

Sakai, J., Matsui, C., Minami, K. (2000). Earthquake Resistant Properties of Core Steel Composite Columns, Proceedings of 12th World Conference on Earthquake Engineering. Auckland.

Mostafa, M.M.A., Wu, T., Liu, X. (2019). Composite Steel Reinforced Concrete Column Under Axial and Seismic Loads: A Review. International Journal of Steel Structures 19.

Farajpourbonab, E. (2019). Development of a new steel section for reinforcing of steel-reinforced concrete-filled steel tubular columns. Structural Concrete, 20: 689-706.

Denavit, M.D., Hajjar, J.F., Perea, T., Leon, R.T. (2018). Elastic flexural rigidity of steel-concrete composite columns. Engineering Structures 160: 293-303.

Papavasileiou, G.S., Charmpis, D.C., Lagaros, N.D. (2020). Optimized seismic retrofit of steel-concrete composite buildings. Engineering Structures 213.

Wang, K., Yuan, S.F., Chen, Z.X., Zhi, H.X., Shi, G.L., Cao, D.F. (2016). Experimental study on hysteretic behavior of composite frames with concrete-encased CFST columns. Journal of Constructional Steel Research 123: 110-20.

Jothimani, B., Umarani, C. (2019). Experimental investigation on concrete filled steel tubular column to foundation connections subjected to combined axial and lateral cyclic loading. Latin American Journal of Solids and Structures 16: e202.

Li, Y.J., Han, L.H., Xu, W., Tao, Z. (2016). Circular concrete-encased concrete-filled steel tube (CFST) stub columns subjected to axial compression. Magazine of Concrete Research 68: 995-1010.

An, Y.F., Han, L.H., Roeder, C. (2014). Flexural performance of concrete-encased concrete-filled steel tubes. Magazine of Concrete Research 66: 249-67.

Lai, B.L., Liew, J.Y.R., Venkateshwaran, A., Li, S., Xiong, M.X. (2020). Assessment of high-strength concrete encased steel composite columns subject to axial compression. Journal of Constructional Steel Research 164: 105765.

Ma, D.Y., Han, L.H., Li, W., Zhao, X.L. (2018). Seismic Performance of Concrete-Encased CFST Piers: Analysis. Journal of Bridge Engineering 23: 04017119.

JGJ 138-2016. (2016). Ministry of Housing and Urban-Rural Development of the People's Republic of China. Code for Design of Composite Structures.

Wang, K., Luo, H.H., Guo, K., Zhou, J., Ma, H.W. (2021). Seismic collapse resistance performance on out-jacketing frames with concrete-encased CFST columns for adding storeys. Structures 33: 41-53.

Hwang, H.J., Eom, T.S., Park, H.G., Lee, S.H., Kim, H.S. (2015). Cyclic loading test for beam-column connections of concrete-filled U-shaped steel beams and concrete-encased steel angle columns. Journal of Structural Engineering 141: 04015020.

Kim, C.S., Hwang, H.J. (2018). Numerical Investigation on Load-carrying Capacity of High-strength Concrete-encased Steel Angle Columns. International Journal of Concrete Structures and Materials 12: 1-17.

Lei, Z.X., Han, Y.H., Dong, S.S., Guo, J.Q. (2013). Analysis of Seismic Performance of RC Frames with Centrally Reinforced Columns. Advanced Materials Research 671-671: 1319-23.

Xing, G.H., Wang, H.N., Osman E, O. (2022). Seismic behavior of multiple reinforcement, high-strength concrete columns: experimental and theoretical analysis. Earthquake Engineering and Engineering Vibration 33: 359-375.

Ye, M., Pi, Y.P., Ren, M. (2012). Preliminary Experimental Study of the Seismic Behavior of Reinforced Concrete Column with Distributed-Steel Bar. Applied Mechanics and Materials 256-259: 2056-62.

Zhao, S.L., Peng, S.L., Zhou, D. (2011). A distributed steel rods connection device. China Patent CN201778400U.

Zhao, S.L., Peng, S.L., Pi, Y.P., Zhou, D., Ren, M., Deng, Y.Q., Wang, Y.J. (2012). Seismic performance study on steel reinforced concrete columns with distributed steel bars by contrast experiment. Building Structure 42: 95-8. (In Chinese).

Chen, G.X. (2012). Comparative experimental research on earthquake-resistant behavior of steel rods reinforced high-strength concrete columns, Master Thesis (In Chinese), South China University of Technology, China.

JGJ 3-2010. (2010). Ministry of Housing and Urban-Rural Development of the People's Republic of China. Technical specification for concrete structures of tall building.

GB 50010-2010. (2010). Ministry of Housing and Urban-Rural Development of the People's Republic of China. Code for design of concrete structures.

ASTM A370. (2017). American Society for Testing and Materials. Standard test methods and definitions for mechanical testing of steel products.

ASTM E2126-11 (2018). ASTM International. Standard Test Methods for Cyclic (Reversed) Load Test for Shear Resistance of Vertical Elements of the Lateral Force Resisting Systems for Buildings.

GB 50011-2010. (2010). Ministry of Housing and Urban-Rural Development of the People's Republic of China. Code for seismic design of buildings.

Wang, J.H., Sun, Y.P. (2022). Seismic Behaviors and Resilience of Concrete-encased Concrete-Filled Steel Tubular Columns with Debonded High-Strength Rebars: Experiment and Assessment. Journal of Earthquake Engineering: 1-27.

Kamaris, G.S., Skalomenos, K.A., Hatzigeorgiou, G.D., Beskos, D.E. (2016). Seismic damage estimation of in-plane regular steel/concrete composite moment resisting frames. Engineering Structures 115: 67-77.

Park, Y.J., Ang, A.H.S. (1985). Mechanistic Seismic Damage Model for Reinforced Concrete. Journal of Structural Engineering 111: 722-39.

Qi, Z.Y., Jiang, N., Wang, L., Ma, S.C. (2016). Seismic damage model for new type gypsum concrete composite walls. Journal of Vibration and Shock 35: 181-88. (In Chinese).